Article

Photocatalytic CO_2 Reduction and Electrocatalytic H_2 Evolution over Pt(0,II,IV)-Loaded Oxidized Ti Sheets

Ju Hyun Yang [1,2], So Jeong Park [1], Choong Kyun Rhee [1] and Youngku Sohn [1,2,*]

[1] Department of Chemistry, Chungnam National University, Daejeon 34134, Korea; mil03076@naver.com (J.H.Y.); jsjs5921@naver.com (S.J.P.); ckrhee@cnu.ac.kr (C.K.R.)

[2] Department of Chemical Engineering and Applied Chemistry, Chungnam National University, Daejeon 34134, Korea

[*] Correspondence: youngkusohn@cnu.ac.kr; Tel.: +82-(42)-8216548

check for updates

Abstract: Energy recycling and production using abundant atmospheric CO_2 and H_2O have increasingly attracted attention for solving energy and environmental problems. Herein, Pt-loaded Ti sheets were prepared by sputter-deposition and Pt^{4+}-reduction methods, and their catalytic activities on both photocatalytic CO_2 reduction and electrochemical hydrogen evolution were fully demonstrated. The surface chemical states were completely examined by X-ray photoelectron spectroscopy before and after CO_2 reduction. Gas chromatography confirmed that CO, CH_4, and CH_3OH were commonly produced as CO_2 reduction products with total yields up to 87.3, 26.9, and 88.0 μmol/mol, respectively for 700 °C-annealed Ti under UVC irradiation for 13 h. Pt-loading commonly negated the CO_2 reduction yields, but CH_4 selectivity was increased. Electrochemical hydrogen evolution reaction (HER) activity showed the highest activity for sputter-deposited Pt on 400 °C-annealed Ti with a HER current density of 10.5 mA/cm^2 at −0.5 V (vs. Ag/AgCl). The activities of CO_2 reduction and HER were found to be significantly dependent on both the nature of Ti support and the oxidation states (0,II,IV) of overlayer Pt. The present result could provide valuable information for designing efficient Pt/Ti-based CO_2 recycle photocatalysts and electrochemical hydrogen production catalysts.

Keywords: energy recycling; photocatalytic CO_2 reduction; electrochemical hydrogen evolution; Ti oxide; Pt oxidation state

1. Introduction

Recycle energy production using abundant CO_2 and H_2O has been a challenging project for energy and environment solutions. Hydrogen production via water splitting is another useful project for these types of solutions. For CO_2 reduction into fuels, increasing selectivity and production efficiency have been very important issues [1–5]. Many strategies have been employed such as defect controlling [6], crystal facet tailoring [7,8], metal alloys/cocatalysts [9,10], support [11], and hybridization [12]. For hydrogen production, diverse strategies have also been employed [13–16]. Among various metal nanoparticles (NPs) on metal oxide supports such as TiO_2, Pt NP has been the most studied and known to have very high beneficial catalytic activity to CO_2 reduction as well as hydrogen production [17–25]. Fang et al. prepared Pt-loaded TiO_2 spheres (>500 μm) by a modified TiO_2 sol-gel method and microwave-assisted Pt reduction method using ethylene glycol as the reducing agent [19]. They reported CO_2 reduction yields of CO and CH_4 with 18 and 3.5 μmol g^{-1} h^{-1}, respectively. Liu et al. prepared well-dispersed Pt on ultrathin TiO_2 and showed 47 μmol of CH_4 formation and 35 μmol of CO formation after UV light irradiation for 10 h [20]. Zhang et al. reported accumulated CH_4 production yield to be about 2.0 μmol g^{-1} for Pt (0.12 *w/w*%)-loaded TiO_2 catalyst at a reaction

temperature of 342 K for 13 h [21]. Wang et al. prepared ultrafine Pt (0.5–1 nm)/TiO_2 nanostructures on ITO via aerosol chemical vapor deposition for TiO_2 and gas-phase sputtering deposition for Pt NPs [22]. They reported CO_2 photoreduction efficiency of 1361 μmol g^{-1} h^{-1} for CH_4 formation and 200 μmol g^{-1} h^{-1} for CO formation. Kometani et al. tested CO_2 reduction over Pt-loaded TiO_2 under supercritical condition of water and CO_2 at 400 °C and 30 MPa [23]. They reported that CO (35.3 ppm), CH_4 (42.7 ppm), and H_2 (65.3 ppm) were major products, and HCOOH (1.7 μM) and HCHO (0.6 μM) were minor. Xiong et al. showed that CO_2 reduction efficiency was highly dependent on the Pt-loading method, which determined the particle size, distribution, and Pt(0)/Pt(II) ratio [26]. They loaded Pt NPs on TiO_2 with co-exposed {101} and {001} facets by photo-reduction and $NaBH_4$-reduction methods using $Pt(NH_3)_4Cl_2$ or H_2PtCl_6 as precursors. The highest (4.6 μmol g^{-1} h^{-1}) and poorest (0.2 μmol g^{-1} h^{-1}) CH_4 yields were reported for Pt NPs by chemical reduction methods using $Pt(NH_3)_4Cl_2$ and H_2PtCl_6, respectively. For crystal facet effects, Mao et al. reported that TiO_2 with {010} facets showed a higher CO_2 photoreduction performance (1.6 μmol g^{-1} h^{-1} of CH_4) than that (0.8 μmol g^{-1} h^{-1}) of TiO_2 with {001} facets [27]. However, 1% Pt-loading on TiO_2 with {001} facets showed a higher activity (2.6 μmol g^{-1} h^{-1}) than that (1.2 μmol g^{-1} h^{-1}) of Pt-loading on TiO_2 with {010} facets. For catalyst and cocatalyst enhancements, Zhang et al. co-decorated Au and Pt NPs (5–12 nm) on TiO_2 nanofibers (NFs) through an electrospinning method [10]. They reported (0.03 μmol h^{-1})/(0.06 μmol h^{-1}), (0.31 μmol h^{-1})/(0.20 μmol h^{-1}), (0.42 μmol h^{-1})/(0.08 μmol h^{-1}), and (0.57 μmol h^{-1})/(0.09 μmol h^{-1}) of CH_4 production/CO production after UV-irradiation for 3 h for pure TiO_2 NFs, Au/TiO_2 NFs, Pt/TiO_2 NFs, and $Au_{0.25}$/$Pt_{0.75}$/TiO_2 NFs, respectively. The CH_4 production was increased by 14 and 19 times after Pt and $Au_{0.25}$/$Pt_{0.75}$ loadings, respectively. The Pt-TiO_2 based photocatalysts for CO_2 reduction in the previously reported literatures were further discussed in comparison with the present result below.

Pt NPs on TiO_2 has also been a good model system for photocatalytic and electrochemical hydrogen production [28–33]. Briefly, Lian developed Pt^{n+} (n = 0, 2, or 3)-Ti^{3+}/TiO_2 system and showed that the photocatalytic H_2 evolution efficiency was higher than that of metallic Pt-loaded Ti^{3+}/TiO_2 and commercial P25 [33]. They attributed the higher efficiency to well dispersed Pt^{n+}–O species, facilitating a photogenerated charge transfer. Yu et al. prepared Pt-loaded TiO_2 and showed that both H_2 and C_2H_6 products were produced by a photocatalytic reaction in a catalyst-dispersed water system filled with CH_4 gas [29].

Herein, to further investigate the roles of overlayer Pt and Ti supports, we prepared sputter-deposited Pt (Pt-sp) and Pt NPs (using a reducing agent) over oxidized Ti sheets and tested for both photocatalytic CO_2 reduction and electrochemical hydrogen production. Different oxidation states (0,II,IV) of Pt were obtained using two different Pt-loading methods. Different natures of Ti supports were obtained by using different thermal annealing treatments. Two different application tests were employed to examine both positive and negative roles in two different application areas. Thereby, the present results provide very useful information on design of catalysts for energy production via CO_2 reduction and electrochemical hydrogen evolution.

2. Materials and Methods

2.1. Preparation of Sputter-Deposited Pt on Ti Sheets and Pt NP on Ti Sheets

Ti sheets (GR2, 32 mm × 32 mm, 0.1 mm thick) were cleaned by ultrasonication in acetone and isopropyl alcohol repeatedly, and dried under an IR lamp. Afterwards, ozone cleaning (UVC-150 ozone cleaner, Omniscience Co., Yongin, Kyoungki, Korea) was performed for 15 min. Ti sheets were then annealed at 400 or 700 °C for 2 h. After the thermal treatment, the sheets were also repeatedly cleaned by the same procedure above. Pt NPs were prepared by a reduction method using $NaBH_4$ and sodium citrate solution for 24 h at room temperature. After that, the NPs were fully washed and drop-coated on the Ti substrate. The sample was abbreviated as Pt-NP/Ti. Pt deposition on the oxidized Ti sheet was performed by a sputter-coating method with an ionization current of 3 mA for 10 s using a SPT-20 ion sputter coater (COXEM Co., Daejeon, Korea). The calibrated Pt thicknesses

was 0.5 nm, abbreviated as Pt-sp. The samples examined here were bare Ti, Ti (400 °C), Ti (700 °C), Pt-NP/Ti, Pt-NP/Ti (400 °C), Pt-NP/Ti (700 °C), Pt-sp/Ti, Pt-sp/Ti (400 °C), and Pt-sp/Ti (700 °C).

2.2. Characterisation of the Samples

The surface morphology of the sheets before and after CO_2 reduction was examined using a Hitachi S-4800 scanning electron microscope (SEM) (Hitach Ltd., Tokyo, Japan) at an accelerating voltage of 10 kV and a current of 10 mA. The surface chemical states for oxidized Ti sheet and Pt-loaded Ti sheets before and after CO_2 reduction were examined by taking X-ray photoelectron spectra (survey, Pt 4f, Ti 2p, C 1s, and O 1s) using a using a Thermo-VG Scientific K-alpha$^+$ spectrometer (Thermo VG Scientific, Waltham, MA, USA) with a monochromatic Al K_α X-ray source and a hemispherical energy analyzer.

2.3. Photocatalytic CO₂ Reduction and Electrochemical Hydrogen Evolution

The photocatalytic CO_2 reduction was performed in a stainless-steel reactor (volume ~40 mL) with a quartz window (3 mm thick and 45 mm diameter) on top. An oxidized Ti sheet or a Pt-loaded sheet was placed in the reactor with 40 μL (or 5 μL) deionized water beside the sheet. Afterwards, the reactor was fully flushed under a stream of pure (99.999%) CO_2 gas for at least 5 min. After the reactor was filled with CO_2 gas and the inlet and outlet valves were closed. For CO_2 reduction experiment, the reactor was placed under four 15 W UVC (200–280 nm) lamps (a power density of 5.94 mW/cm^2) for 13 h. Blank tests under dark condition were also performed to examine the precise role of light. The CO_2 reduction gas products such as CO, CH_4, and CH_3OH were analyzed by a YL 6500 gas chromatograph (Young In Chromass Co., Ltd., Seoul, Korea) equipped with a Ni catalyst methanizer assembly, a flame ionization detector (FID), and a thermal conductivity detector (TCD). For GC analysis, 0.5 mL volume of gas from the reactor was taken using a gastight syringe to be injected into two different columns of 40/60 Carboxen-1000 (Sigma-Aldrich, St. Louis, MO, USA) and HP-PlotQ-PT (Agilent Technologies, Inc., Santa Clara, CA, USA). Electrochemical hydrogen evolution reaction (HER) tests were performed using a three-electrode system (a Pt counter electrode, a Ag/AgCl reference electrode, and a Ti electrode working electrode) using a WPG100 Potentiostat/Galvanostat (WonATech Co., Ltd., Seoul, Korea) electrochemical workstation. Cyclic voltammetry (CV) and linear sweep voltammetry (LSV) were carried in 0.1 M H_2SO_4 electrolyte solution at a potential range from +0.1 to −0.8 V.

3. Results and Discussion

Figure 1 shows the SEM images for bare Ti, oxidized (400 and 700 °C-annealed) Ti, Pt NP/Ti, Pt NP/Ti (400 °C), Pt NP/Ti (700 °C), Pt-sp/Ti, Pt-sp/Ti (400 °C), and Pt-sp/Ti (700 °C) samples. The surface morphology was found to be mainly determined by thermal treatment temperature and the Pt-prepared conditions. The samples (Figure 1(A2,B2,C2)) treated at 700 °C showed a more crystalline structure on the surface. However, the as-received Ti (Figure 1A) showed a blurred image surface. The 400 °C annealed sample (Figure 1(A1)) showed the morphology between the two. Upon Pt NP loading (prepared using a reducing agent) on the three different surfaces (bare Ti, 400 and 700 °C-annealed Ti), the surface morphology shown was quite distinct. The Pt NPs were aggregated on bare Ti (Figure 1B), while the NPs on 400 and 700 °C-annealed Ti (Figure 1(B1,B2)) sheets were relatively well dispersed. For the sputter-deposited Pt, no discernible particles were found. This could be due to that Pt (0.5 nm thick) was evenly embedded to form Pt-O species, which was confirmed by XPS below.
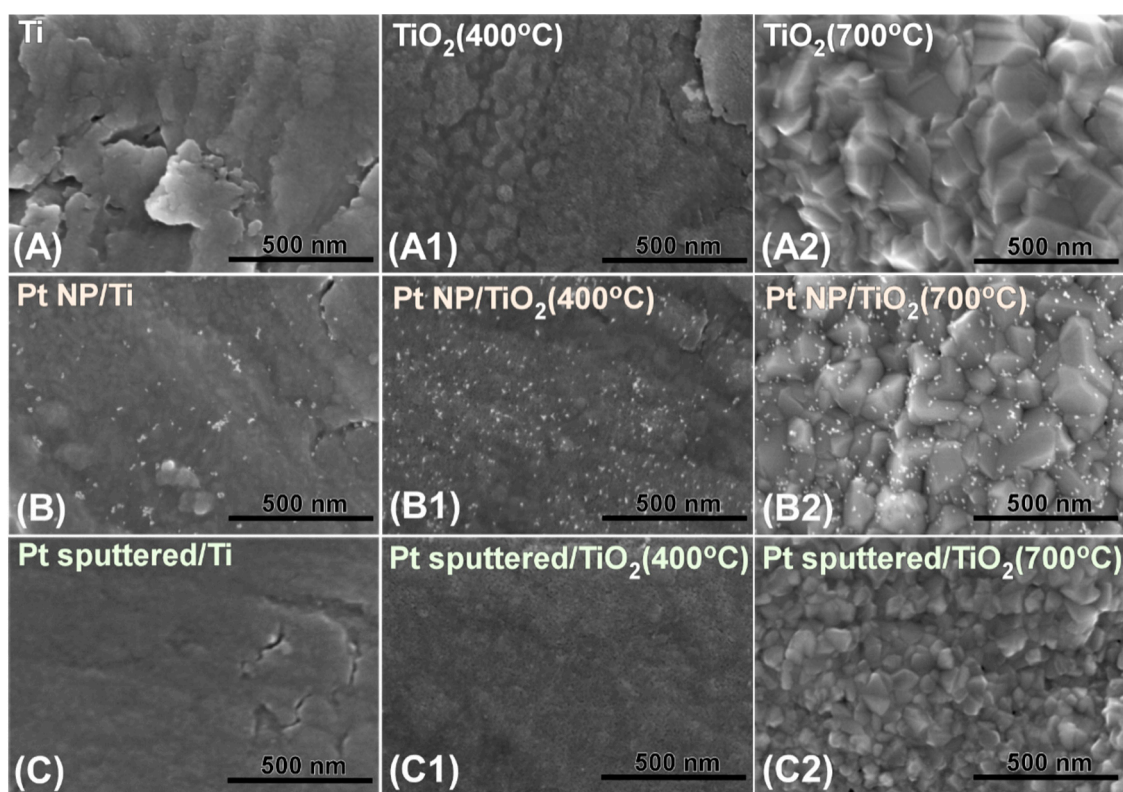
Figure 1. Scanning electron microscope (SEM) images of: (**A**) bare Ti; (**A1**) bare Ti (400 °C); (**A2**) bare Ti (700 °C); (**B**) Pt NP/Ti; (**B1**) Pt NP/Ti (400 °C); (**B2**) Pt NP/Ti (700 °C); (**C**) Pt-sp/Ti; (**C1**) Pt-sp/Ti (400 °C); (**C2**) Pt-sp/Ti (700 °C) samples.

For photocatalytic CO_2 reduction, the design of a photoreactor system is also very important [1]. Two general photoreactor systems have been employed, which are (1) catalyst dispersed in a CO_2-saturated aqueous liquid: solid-liquid mode, and (2) catalyst dispersed on a support with gaseous CO_2 and H_2O: solid-gas mode. In the present study, the solid (catalyst)-gas (CO_2 + H_2O) system was employed. CO_2 reduction products were examined and displayed in Figure 2. Carbon monoxide (CO), methane (CH_4), and methanol (CH_3OH) were commonly been produced with different yields for bare Ti, Ti (400 °C), bare Ti (700 °C), Pt NP/Ti, Pt NP/Ti (400 °C), Pt NP/Ti (700 °C), Pt-sp/Ti, Pt-sp/Ti (400 °C), and Pt-sp/Ti (700 °C) sheets. For bare Ti, it was found that total CO, CH_3OH, and CH_4 production yields (μmol/mol = ppm) after UVC irradiation for 13 h were observed to be 81.3, 67.1, and 19.5 ppm, respectively. These yields became substantially decreased to 32.3, 0, and 8.7 ppm, respectively for Ti (400 °C) sheet. However, for 700 °C-annealed Ti, CO, CH_3OH, and CH_4 production yields became again increased to 87.3, 88.0, and 26.9 ppm, respectively. The CO/CH_4 production ratios were estimated to be 4.2, 3.7, and 3.2 for bare Ti, Ti (400 °C), and Ti (700 °C), respectively. For bare Pt-free Ti substrates, the activity showed the order of Ti (400 °C) < Ti < bare Ti (700 °C). The Ti (700 °C) sheet showed the highest CO_2 reduction activity. This indicates that the nature of Ti surface mainly determines the activity. Upon Pt-loading, the CO_2 reduction yields were commonly diminished, but the CH_4 production was less impacted. For Pt NP on Ti, the CO and CH_3OH productions were decreased by 47% and 68%, respectively. However, CH_4 production was increased by 14%. For sputter-deposited Pt on Ti, the CO, CH_3OH, and CH_4 productions were decreased by 48%, 26%, and 19%, respectively. For Pt NP on Ti (400 °C), CO and CH_4 yields were observed to be 2.1 and 12.7 ppm, respectively compared with those of bare Ti (400 °C) sheet. CO yield was substantially decreased by 93%, but the CH_4 yield was increased by 45%. For sputter-deposited Pt on Ti (400 °C), no CO was detected, and CH_3OH and CH_4 production yields were merely observed to be 1.6 and 7.9 ppm. For the Pt-loading on Ti (700 °C) sheet, the CO_2 reduction activity was more severely impacted. CO, CH_3OH, and CH_4

production yields were decreased by 82%, 50%, and 41%, respectively. For the sputter-deposited Pt on Ti (700 °C), CO, CH₃OH and CH₄ production yields were more significantly decreased by 98%, 92%, and 38%, respectively. The CO/CH₄ production ratios were estimated to be 0.16, 1.0, and 1.9 for Pt NP/Ti, Pt NP/Ti (400 °C), and Pt NP/Ti (700 °C), respectively. For Pt-sp/Ti, Pt-sp/Ti (400 °C), and Pt-sp/Ti (700 °C), the CO/CH₄ production ratios were estimated to be 0.0, 0.1, and 2.7, respectively. CH₄ selectivity was commonly increased upon Pt-loading.
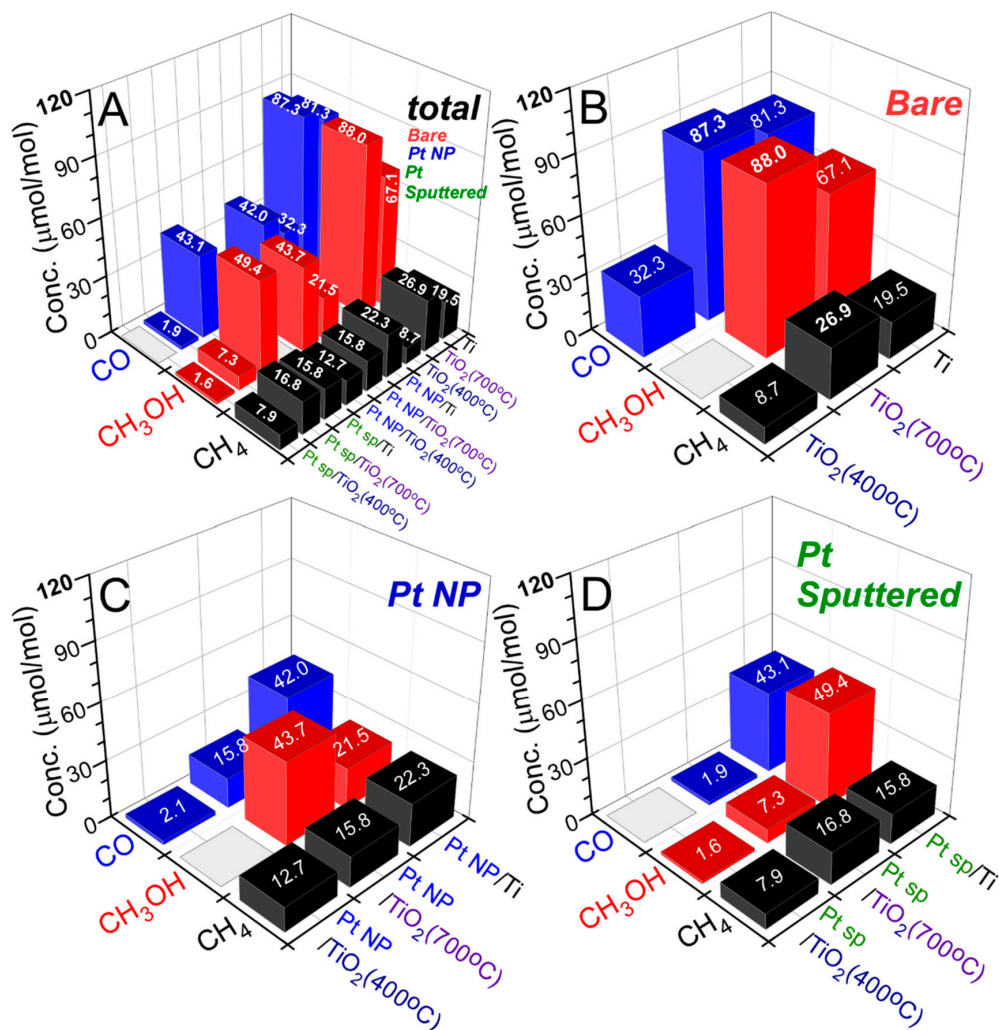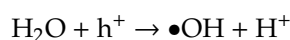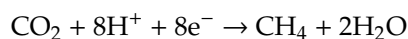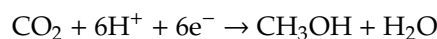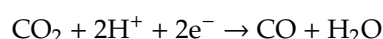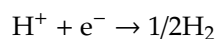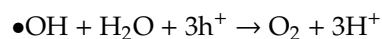

Figure 2. CO_2 reduction (CO, CH_4, and CH_3OH) yields (μmol/mol) over: (**B**) bare Ti, Ti (400 °C), and Ti (700 °C); (**C**) Pt NP/Ti, Pt NP/Ti (400 °C), and Pt NP/Ti (700 °C); (**D**) Pt-sp/Ti, Pt-sp/Ti (400 °C), and Pt-sp/Ti (700 °C) samples. (**A**) is the total plot for (**B**–**D**).

CO_2 reduction mechanism is highly dependent on the production of protons and electrons [1,10]. The general equation is written as $xCO_2 + yH^+ + ze^- \rightarrow C_n$ products $+ mH_2O$, where C_n is an organic compound. Under UV irradiation, electrons (e^-) and holes (h^+) are created in the conduction and valence bands (CB and VB), respectively. Because CO_2 reduction occurs through multielectron processes, the creation of photogenerated electrons is an important factor for the catalytic activity. The photogenerated electrons and holes are separated to participate in several reactions described below:

$$TiO_2 + h\nu \rightarrow TiO_2 \text{ (VB, } h^+) + TiO_2 \text{ (CB, } e^-)$$

$$H_2O + h^+ \rightarrow \bullet OH + H^+$$

$$\bullet OH + H_2O + 3h^+ \rightarrow O_2 + 3H^+$$

$$H^+ + e^- \rightarrow 1/2H_2$$

$$CO_2 + 2H^+ + 2e^- \rightarrow CO + H_2O$$

$$CO + 6H^+ + 6e^- \rightarrow CH_4 + H_2O$$

$$CO_2 + 6H^+ + 6e^- \rightarrow CH_3OH + H_2O$$

$$CO_2 + 8H^+ + 8e^- \rightarrow CH_4 + 2H_2O$$
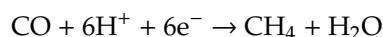
In the CO_2 reduction mechanism, several reaction channels are closely spaced and diverse products of CO, CH_4, and CH_3OH are obtained via multielectron processes described above. Notably, kinetically favored hydrogen production channel is also among the CO_2 reduction channels. Therefore, H^+ and e^- can be consumed for H_2 production. As discussed above, when Pt species were present, CO_2 reduction was observed to be negated and photocatalytic hydrogen production was increased.

In Table 1, we have summarized Pt-TiO$_2$ based photocatalysts for CO_2 reduction in the previously reported literatures [10,17,19–22,24,27,34–37]. CO and CH_4 have commonly been observed as CO_2 reduction products, consistent with the present results. Generally, the yield of CH_4 was reported to be higher than that of CO, although the reaction conditions (e.g., light intensity, wavelength, water amount, and reactor type) were all different. In the present result, CH_4 production over Pt-loaded Ti oxides was also observed to be higher than CO production, which was consistent with the literature. This indicates that the CH_4 production channel became superior to the CO production channel upon Pt-loading, which is discussed further below.

Table 1. Photoreactor conditions and reduction yields for reported Pt/Ti-oxide-based catalysts.

Pt/Ti-Oxide Catalysts [Reference]	Photoreactor Conditions	Major Products and Yields
1% Pt-loading on TiO$_2$ with {001} facets [27]	300 W Hg-lamp, 0.1 g on 28 cm^2 watch glass in 350 mL reactor	CH_4: 2.6 µmol g^{-1} h^{-1} No CO
Pt (0.2 wt.%)/TiO$_2$: impregnation and thermal treatment [34]	0.1 g catalyst, 423 K, 400 W Hg lamp, CO_2 flow (4.5 mL/min) saturated with H$_2$O vapor	CH_4: 1.46 µmol g^{-1} h^{-1} H$_2$: 5.28 µmol g^{-1} h^{-1}
Pt (1.82 nm)/TiO$_2$ NPs [24]	132 mL stainless steel reactor, 500 W Xe lamp, 20 mg catalyst, 5 mL H$_2$O	CH_4: 60.1 µmol g^{-1} h^{-1} C$_2$H$_6$: 2.8 µmol g^{-1} h^{-1} H$_2$: 87.5 µmol g^{-1} h^{-1}
1.5 wt.% Pt/TiO$_2$ photocatalyst [35]	UV 8 W Hg lamp (peak intensity at 254 nm) 0.1 g catalyst, 10 mL H$_2$O, Pressured CO_2 in the 348 mL reactor	CO: 7 µmol g^{-1} for 12 h CH_4: 15 µmol g^{-1} for 12 h H$_2$: 270 µmol g^{-1} for 12 h
Pt (3–4 nm)/TiO$_2$ nanosheet porous film [36]	300 W Hg lamp (10.4 mW/cm^2) 20 mL 0.1 mol/L KHCO$_3$ solution	CH_4: 20.5 ppm cm^{-1} h^{-1}
Pt on ultrathin TiO$_2$ [20]	10 mg catalyst, 50 cm^3 of chamber volume. 300 W Xe lamp	CH_4: 47 µmol for 10 h CO: 35 µmol for 10 h
Pt-loaded TiO$_2$ spheres (>500 µm) [19]	200 mg catalyst, 100 µL of DI water, pressurized CO_2 (50 PSI), UV (20 mW/cm^2, 254 nm)	CO: 18 µmol g^{-1} h^{-1} CH_4: 3.5 µmol g^{-1} h^{-1} H$_2$: 230 µmol g^{-1} h^{-1}
Pt NPs (5–12 nm) on TiO$_2$ nanofibers through electrospinning [10]	5 mg catalyst on 2 cm × 2 cm glass, 500 W Xe lamp, 0.1 mL of deionized water, 90 mL gastight reactor	CO: 0.08 µmol h^{-1} CH_4: 0.42 µmol g^{-1} h^{-1}
Pt^{2+}–Pt^0/TiO$_2$ NPs by sol-gel method [37]	300 W Xe arc lamp, 0.1 g on glass-fiber cloth in 85 mL reactor, a mixture of CO_2, and water vapor flow	CO: 20 µmol g^{-1} for 14 h CH_4: 264 µmol g^{-1} for 7 h H$_2$: 2763 µmol g^{-1} for 7 h

<div align="center">Table 1. Cont.</div>

Pt/Ti-Oxide Catalysts [Reference]	Photoreactor Conditions	Major Products and Yields
Sputter deposited Pt (1 nm) on TiO_2 by aerosol chemical vapor deposition [22]	400 W Xe lamp (250–388 nm, 19.6 mW/cm^2), a mixture of CO_2 and water vapor, flow reactor system	CH_4: 1361 µmol g^{-1} h^{-1} CO: 200 µmol g^{-1} h^{-1}
Platinum-impregnated P25, Pt/TiO_2 [17]	UV-curing 100 W high-pressure Hg lamp (170 mW cm^{-2}), 353 and 423 K, gas-phase continuous flow reactor.	CH_4: 1.08 µmol g^{-1} h^{-1} H_2: 11.4 µmol g^{-1} h^{-1}
Pt/TiO_2 nanotube [21]	a 300 W high-pressure Hg lamp (wavelength 365 nm), a fixed-bed photocatalysis reactor, 50 mg on the flat quartz plate	CH_4 yield with 0.0565 µmol h^{-1} g^{-1} after 7 h UV irradiation.

The surface oxidation states were examined by obtaining X-ray photoelectron spectroscopy (XPS) data before and after photocatalytic CO_2 reduction. All the XPS peaks were deconvoluted for the clear identification of several oxidation states. The relative peak ratios are provided in the inset table in each Figures 3–6. Figure 3 shows Ti 2p and O 1s XPS profiles for Pt-free Ti, Ti (400 °C), and Ti (700 °C) samples. The Ti 2p profiles were quite similar before and after CO_2 reduction. For the Ti 2p XPS for bare Ti in Figure 3A, several peaks were observed at binding energies (BEs) of 454.8, 458.8, and 464.6 eV, and between these peaks. The Ti 2p$_{1/2}$ and Ti 2p$_{3/2}$ peaks were observed at BEs of 464.6 and 458.8 eV, respectively with a spin-orbit splitting of 5.8 eV. This is attributed to Ti(IV) state of TiO_2 [38–40]. Other Ti 2p$_{1/2}$ and Ti 2p$_{3/2}$ peaks were observed around 460.8 and 454.8 eV, respectively. This is attributed to Ti(II) of TiC [38–40] whose corresponding C 1s peak was observed at 281.9 eV. In addition, the broadly distributed Ti 2p$_{3/2}$ signals between 454.8 and 459.0 eV could be due to Ti(II,III) oxidation states. For the 400 °C-annealed Ti in Figure 3(A1), substantial change in Ti 2p peak was observed, the Ti 2p$_{1/2}$ and Ti 2p$_{3/2}$ peaks were observed only at BEs of 464.9 and 459.3 eV, respectively. No Ti 2p signals of Ti(II) and Ti(III) species were observed. This indicates that all Ti(II) and Ti(III) species were oxidized to Ti(IV). For the 700 °C-annealed Ti in Figure 3(A2), the Ti 2p$_{1/2}$ and Ti 2p$_{3/2}$ peaks were observed only at BEs of 464.6 and 459.0 eV, respectively. The BEs were shifted by 0.3 eV to a lower BE position, compared with those for the 400 °C-annealed Ti. This implies that the acidity of Ti^{4+} site became lower upon 700 °C annealing.
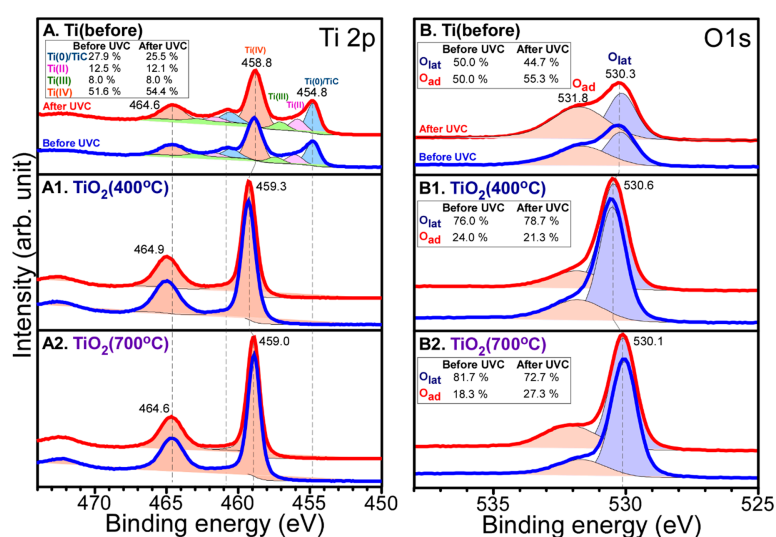

Figure 3. Ti 2p (left column) and O 1s (right column) XPS of: (**A,B**) bare Ti; (**A1,B1**) Ti (400 °C); (**A2,B2**) Ti (700 °C) before (blue) and after (red) CO_2 reduction. The dot lines are normalized peaks for comparison before and after CO_2 reduction. Inset tables show relative ratios of the deconvoluted peaks.
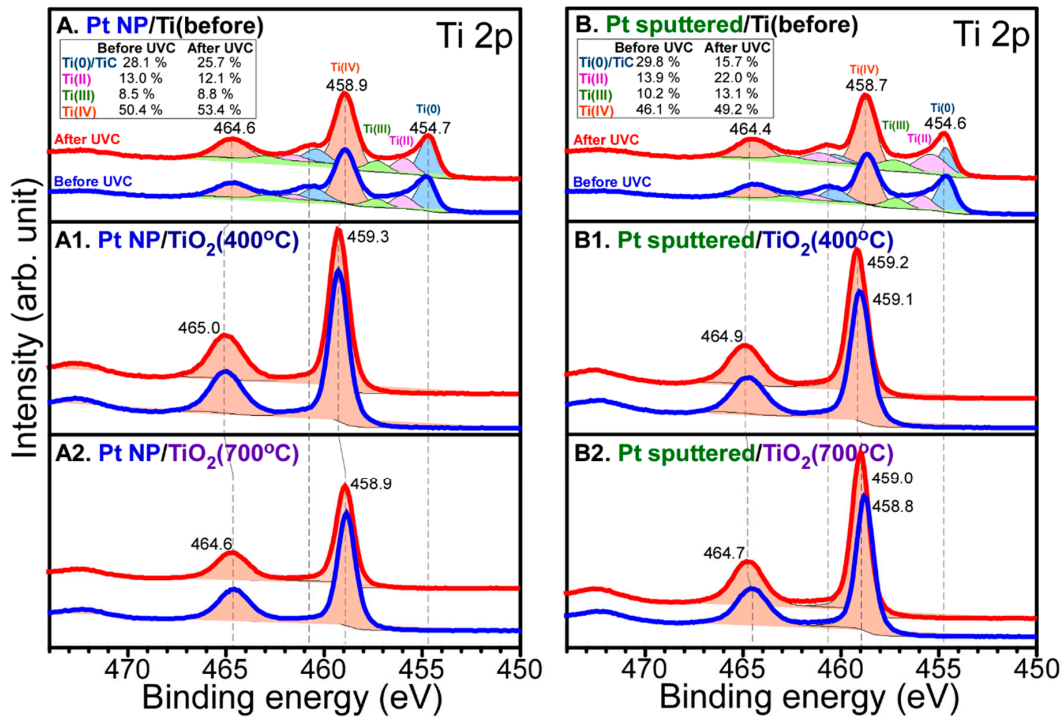
Figure 4. Ti 2p XPS of: (**A**) Pt NP/Ti; (**A1**) Pt NP/Ti (400 °C); (**A2**) Pt NP/Ti (700 °C); (**B**) Pt-sp/Ti; (**B1**) Pt-sp/Ti (400 °C); (**B2**) Pt-sp/Ti (700 °C) samples before (blue) and after (red) CO_2 reduction. Inset tables show relative ratios of the deconvoluted peaks.

Figure 5. O 1s XPS of: (**A**) Pt NP/Ti; (**A1**) Pt NP/Ti (400 °C); (**A2**) Pt NP/Ti (700 °C); (**B**) Pt-sp/Ti; (**B1**) Pt-sp/Ti (400 °C); (**B2**) Pt-sp/Ti (700 °C) samples before (blue) and after (red) CO_2 reduction. Inset tables show relative ratios of the deconvoluted peaks.
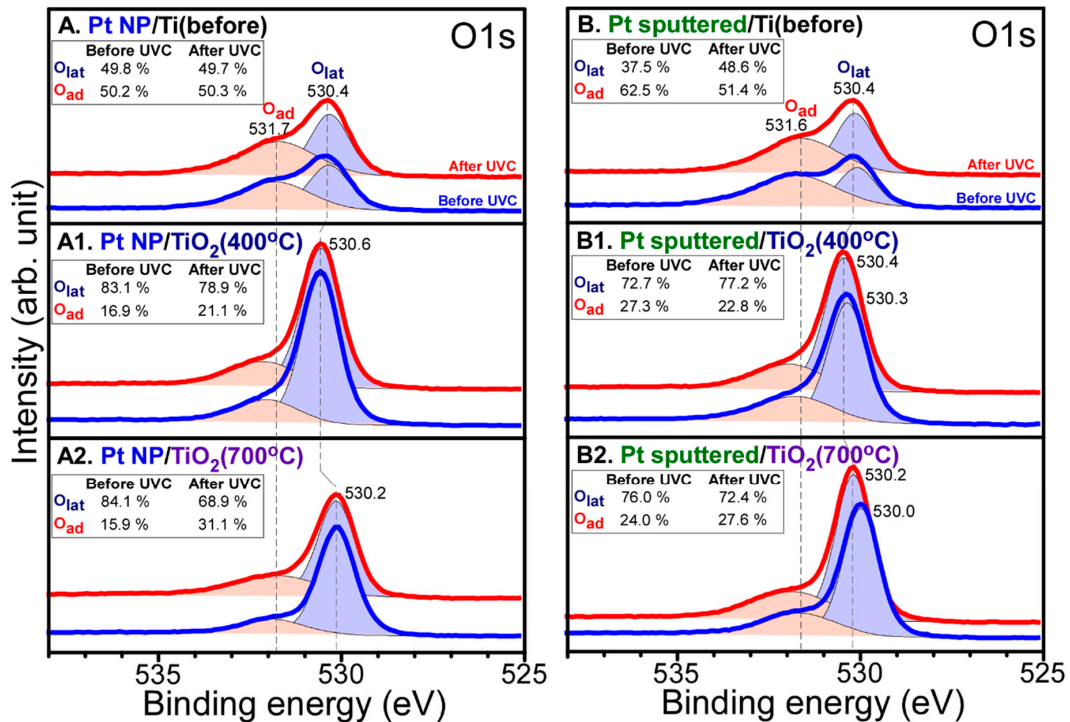
Figure 6. Pt 4f XPS of: (**A**) Pt NP/Ti; (**A1**) Pt NP/Ti (400 °C); (**A2**) Pt NP/Ti (700 °C); (**B**) Pt-sp/Ti; (**B1**) Pt-sp/Ti (400 °C); (**B2**) Pt-sp/Ti (700 °C) samples before (blue) and after (red) CO_2 reduction. Inset tables show relative ratios of the deconvoluted peaks.
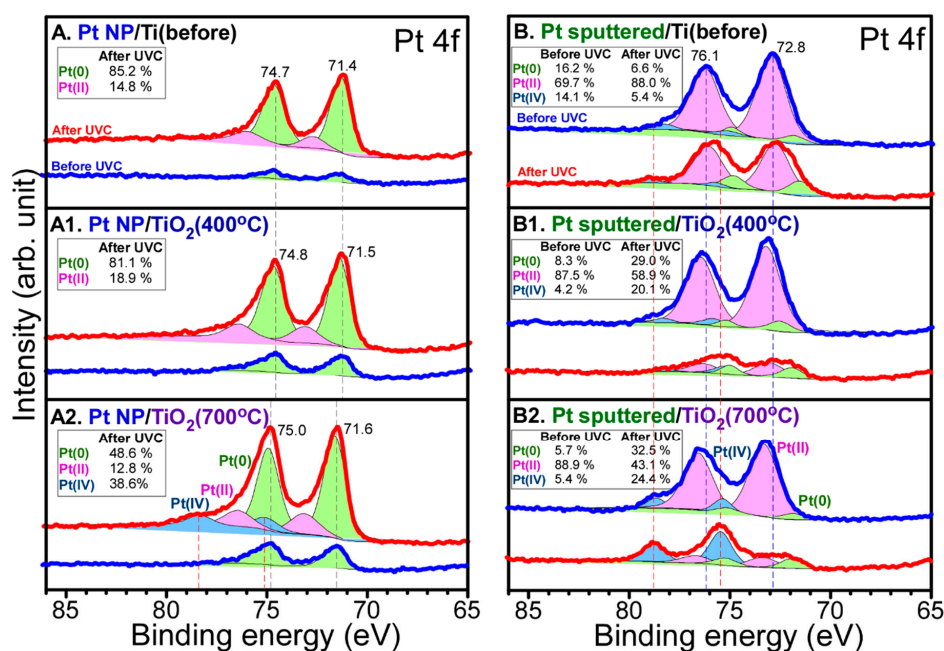
For the O 1s X-ray photoelectron (XP) spectra of Pt-free Ti, Ti (400 °C) and Ti (700 °C) samples before and after CO_2 reduction, two broad regions were commonly observed, and the lower and higher BE peaks were attributed to lattice oxygen (O_{lat}) and adsorbed surface oxygen species (O_{ad}), respectively [29,39–41]. The O_{ad}/O_{lat} ratio of Ti sample in Figure 3B was found to be much higher than those of Ti (400 °C) and Ti (700 °C) samples, as expected. The O 1s XP BE positions for lattice oxygen were observed to be 530.3, 530.6 and 530.1 eV for Ti, Ti (400 °C) and Ti (700 °C) samples, respectively. However, the O 1s XP BE positions for surface oxygen species were found to be similar for the three different samples. For the O 1s of the Ti (400 °C) sample in Figure 3(B1), the O_{ad}/O_{lat} ratio was somewhat decreased after CO_2 reduction. However, the O_{ad}/O_{lat} ratio was increased to be higher for Ti and Ti (700 °C) samples after CO_2 reduction in Figure 3(B2). This reflects higher CO_2 reduction activity for Ti and Ti (700 °C) samples, compared with the Ti (400 °C) sample. This is in good consistent with the data shown in Figure 2B.

Figure 4 shows Ti 2p XPS for Pt NP/Ti, Pt NP/Ti (400 °C), Pt NP/Ti (700 °C), Pt-sp/Ti, Pt-sp/Ti (400 °C), and Pt-sp/Ti (700 °C) samples before and after CO_2 reduction. For the Ti 2p XPS for Pt NP/Ti in Figure 4A, several peaks were observed at binding energies (BEs) of 454.7, 458.9, 464.6 eV, and between these peaks, as observed above. The Ti $2p_{1/2}$ and Ti $2p_{3/2}$ peaks were observed at BEs of 464.6 and 458.9 eV, respectively with a spin-orbit splitting of 5.7 eV. This is attributed to Ti(IV) state of TiO_2 [38–40]. Other Ti $2p_{1/2}$ and Ti $2p_{3/2}$ peaks were observed around 460.8 and 454.7 eV, respectively. This is attributed to Ti(II) of TiC, as mentioned above [38–40]. In addition, the broadly distributed Ti $2p_{3/2}$ signals between 454.7 and 459.0 eV could be due to Ti(II,III) oxidation states. The Ti 2p XPS showed no critical change after CO_2 reduction. For the Ti 2p XPS for Pt-sp/Ti in Figure 4B, the Ti 2p XPS profiles were quite similar to those for Pt NP/Ti in Figure 4A. For the Ti 2p XPS for Pt NP/Ti (400 °C) before and after CO_2 reduction in Figure 4(A1), it was clear that the Ti 2p signals of Ti(0), Ti(II), and Ti(III) completely disappeared. This indicates that all the species were changed to Ti(IV) upon thermal annealing at 400 °C. The Ti $2p_{1/2}$ and Ti $2p_{3/2}$ peaks were observed at BEs of 465.0 and 459.3 eV, respectively. The BE was shifted by +0.4 eV to a higher BE position. For the Ti 2p XPS for Pt-sp/(400 °C) in Figure 4(B1), the Ti 2p XPS profiles were also quite similar to those for Pt NP/(400 °C) in Figure 4(A1). For the Ti 2p XPS for Pt NP/Ti (700 °C) before and after CO_2 reduction in Figure 4(A2), the Ti $2p_{1/2}$ and

Ti $2p_{3/2}$ peaks were observed at BEs of 464.6 and 458.9 eV, respectively. The BE was shifted by 0.4 eV to a lower BE position, compared with that for the Ti 2p XPS of Pt NP/Ti (400 °C). This indicates that the acidity of Ti^{4+} site became lower upon annealing at a higher temperature. The Ti 2p XPS showed no big change after CO_2 reduction experiment. For the Ti 2p XPS for Pt-sp/(700 °C) in Figure 4(B2), the Ti 2p XPS profiles were quite similar to those for Pt NP/(700 °C) in Figure 4(A2). On the basis of the Ti 2p XPS results, the natures of Ti sites were quite different for all the samples, meaning that different CO_2 reduction and HER activities were expected, as discussed above and below.

Figure 5 displays O 1s XP spectra for Pt NP/Ti, Pt NP/Ti (400 °C), Pt NP/Ti (700 °C), Pt-sp/Ti, Pt-sp/Ti (400 °C), and Pt-sp/Ti (700 °C) samples before and after CO_2 reduction. Two broad regions were commonly observed as discussed above, and the lower and higher BE peaks were attributed to lattice oxygen (O_{lat}) and adsorbed surface oxygen species (O_{ad}), respectively [29,39–41]. The O_{ad}/O_{lat} ratios of Pt NP/Ti and Pt-sp/Ti samples were much higher than those of corresponding Ti (400 °C) and Ti (700 °C) samples, due to a thermal treatment effect. The O 1s XP BE positions for lattice oxygen were observed to be 530.4, 530.6, and 530.2 eV for Pt NP/Ti, Pt NP/Ti (400 °C) and Pt NP/Ti (700 °C) samples, respectively. For Pt-sp/Ti, Pt-sp/Ti (400 °C), and Pt-sp/Ti (700 °C) samples, the O 1s XP BE positions were observed to be 530.2, 530.3, and 530.0 eV, respectively. However, the O 1s XP BE positions for surface oxygen species were found to be similar for the three different samples. A major difference in the O 1s profile after CO_2 reduction was found in the intensity of adsorbed surface oxygen species. The Pt NP/Ti (400 °C) and Pt-sp/Ti (400 °C) samples showed minimal change in the intensity of adsorbed surface oxygen species after CO_2 reduction, compared with other samples. This reflects that as discussed above, the Ti (400 °C) samples showed the lowest CO_2 reduction activity, consistent with the data shown in Figure 2C,D.

Figure 6 displays Pt 4f XP spectra for Pt NP/Ti, Pt NP/Ti (400 °C), Pt NP/Ti (700 °C), Pt-sp/Ti, Pt-sp/Ti (400 °C), and Pt-sp/Ti (700 °C) samples before and after CO_2 reduction. For the Pt NP-loaded samples before CO_2 reduction, two major peaks were observed at 75.0 and 71.6 eV for Pt NP/Ti (700 °C), attributed to Pt $4f_{5/2}$ and Pt $4f_{7/2}$ XPS peaks of metallic Pt, respectively [29,40]. The Pt NP/Ti sample showed at BEs of 74.7 and 71.4 eV for Pt $4f_{5/2}$ and Pt $4f_{7/2}$ XPS peaks. The Pt $4f_{5/2}$ and Pt $4f_{7/2}$ XPS peaks for the Pt NP/Ti (400 °C) showed BEs of 74.8 and 71.5 eV, respectively. After CO_2 reduction, the major BE position showed no critical change, but the XPS signals above 75 eV were slightly enhanced. This reflects an increase in Pt^{4+} species showing BEs at 78.8 and 75.3 eV for Pt $4f_{5/2}$ and Pt $4f_{7/2}$ XPS peaks. For the sputtered-Pt samples before CO_2 reduction, a big difference in BE position was found. Two major peaks at 76.6 and 73.3 eV were found for Pt-sp/Ti (700 °C) sample, attributed to Pt $4f_{5/2}$ and Pt $4f_{7/2}$ XPS peaks of Pt(II), respectively [29]. In addition, smaller peaks were observed at 78.7 and 75.4 eV, attributed to Pt $4f_{5/2}$ and Pt $4f_{7/2}$ XPS peaks of Pt(IV), respectively. Metallic Pt was weakly seen in the spectra [20,41]. This indicates that sputtered Pt were of Pt(II) and Pt(IV) species co-existed as oxidized Pt species. For the Pt-sp/Ti samples before CO_2 reduction, two major peaks were found at 76.1 and 72.8 eV. For Pt-sp/Ti (400 °C) before CO_2 reduction, two major peaks were found at 76.4 and 73.1 eV. The Ti support annealed at a higher temperature showed higher BE position for the Pt $4f_{5/2}$ and Pt $4f_{7/2}$ XPS peaks of Pt(II). For the Pt-sp/Ti samples after CO_2 reduction, Pt(II) oxidation species were decreased while Pt(IV) and Pt(0) species were observed to be increased. The change in Pt 4f became more distinct for the Ti support annealed at a higher temperature. For the Pt-sp/Ti (700 °C) sample, Pt(IV) species became dominant and the corresponding Pt $4f_{5/2}$ and Pt $4f_{7/2}$ XPS peaks were found at 78.7 and 75.4 eV. For the Ti (700 °C) support, Pt(IV) species were commonly observed to be higher than other Ti supports.

For hydrogen production in a three-electrode electrochemical system, electrochemical linear sweep voltammetry (LSV) was tested to examine electrocatalytic hydrogen evolution reaction (HER) activities for Pt wire, bare Ti, oxidized (400 and 700 °C-annealed) Ti, Pt NP/Ti, Pt NP/Ti (400 °C), Pt NP/Ti (700 °C), Pt-sp/Ti, Pt-sp/Ti (400 °C), and Pt-sp/Ti (700 °C) samples. Pt has popularly been used for hydrogen production and shown good catalytic activity [13–16,42]. Figure 7 displays the corresponding LSV data (between 0.0 and −0.8 V vs. Ag/AgCl) obtained in 0.1 M H_2SO_4 solution. The corresponding current

density (CD, mA/cm^2) taken at -0.5 V was also plotted for direct comparison of the HER activity. It was clearly shown that the CD was found to be considerably dependent on the Pt-loading and thermal treatment temperature of Ti support. The Pt-free bare Ti, Ti (400 °C), and Ti (700 °C) samples showed the poorest activity, showing onset potentials above -0.6 V, compared with Pt-loaded samples. HER CDs were observed to be 0.07, 0.1, and 0.07 mA/cm^2 at -0.5 V (vs. Ag/AgCl) for Ti, Ti (400 °C), and Ti (700 °C) samples, respectively. For a Pt wire, the onset potential was observed around -0.22 V. For the Pt-loaded Ti and Ti (400 °C) samples (Figure 7A,B, respectively) showed the onset potentials close to that of a Pt wire. However, the Pt-loaded Ti (700 °C) samples (Figure 7C) showed much higher HER onset potential of -0.5 V. This indicates that the HER activity was shown to be much poorer than those of Pt-loaded Ti and Ti (400 °C) samples. The HER activity showed the order of Ti (700 °C) < Ti < Ti (400 °C), whose order was inverse to the CO_2 reduction. The Ti (400 °C) support showed the highest HER activity and increased upon Pt-loading. This is a clear evidence that catalyst support is very important for improving catalytic activity. For Pt-NP loaded samples, HER CDs were observed to be 4.1, 9.6, and 0.09 mA/cm^2 at -0.5 V (vs. Ag/AgCl) for Pt-NP/Ti, Pt-NP/Ti (400 °C), and Pt-NP/Ti (700 °C), respectively. For sputtered Pt-loaded samples, HER CDs were observed to be 7.6, 10.5, and 1.1 mA/cm^2 at -0.5 V (vs. Ag/AgCl), Pt-sp/Ti, Pt-sp/Ti (400 °C), and Pt-sp/Ti (700 °C), respectively. It was common that the sputtered Pt-loaded samples showed higher HER activity compared with the corresponding Pt-NP loaded samples, in good agreement with the literature [33]. Lian et al. also observed same for H_2 evolution efficiency tests over Pt^{n+} (n = 0, 2, or 3)-Ti^{3+}/TiO_2 and metallic Pt-loaded Ti^{3+}/TiO_2 [33]. XPS data (Figure 6) and HER activity (Figure 7) clearly confirms that the oxidation state of overlayer Pt plays a significant role in improving HER activity. In addition, when the TiO_2 layer is too thick (in case of the 700 °C-treated samples) the HER activity becomes poor because of poor electrical current flow in an electrochemical reaction.
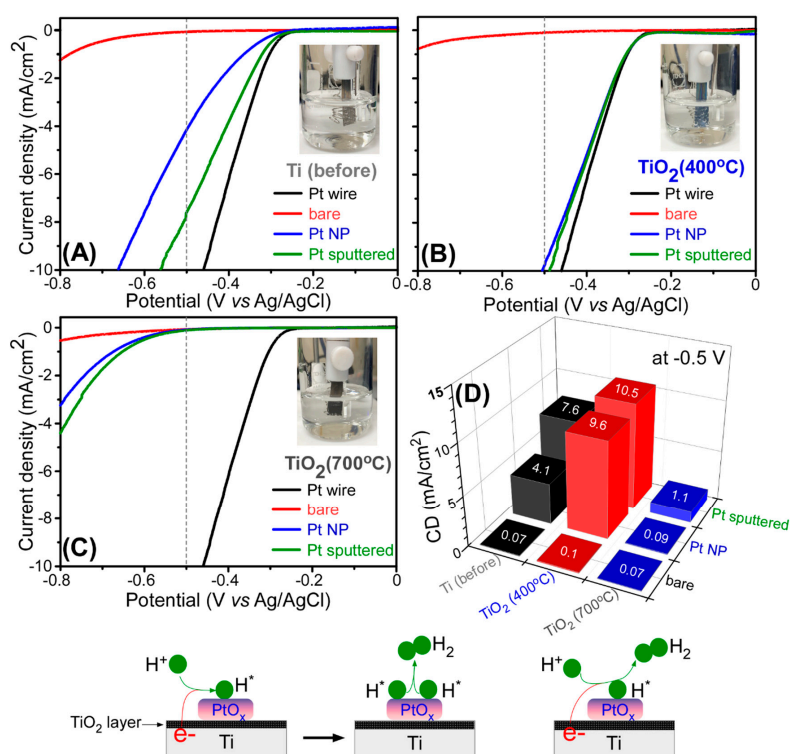

Figure 7. Linear sweep voltammetry (LSV) data at a scan rate of 10 mV/s for: (**A**) bare Ti, Ti (400 °C) and Ti (700 °C); (**B**) Pt NP/Ti, Pt NP/Ti (400 °C) and Pt NP/Ti (700 °C); (**C**) Pt-sp/Ti, Pt-sp/Ti (400 °C) and Pt-sp/Ti (700 °C) samples, and for Pt wire (blank line); (**D**) current density (mA/cm^2) taken at -0.5 V for the corresponding samples. The HER mechanism is depicted below.

For the HER mechanism in acidic media, hydrogen is adsorbed on the catalyst surface via H_3O^+ + $e^- \rightarrow H_{ad} + H_2O$. Then, molecular hydrogen is released from the surface via $H_{ad} + H_3O^+ + e^- \rightarrow H_2 + H_2O$ or $H_{ad} + H_{ad} \rightarrow H_2$ [43–45]. The mechanism is depicted in Figure 7, where the adsorption of H occurs on (or periphery of) PtO_x or Pt NPs species. When hydrogen adsorption Gibbs free energy, ΔG_{HX} is closer to 0 eV the HER activity become higher. When Pt (or PtO_x) is present, the ΔG_{HX} appears to be close to 0 and the HER activity becomes enhanced [43–45]. The ΔG_{HX} is determined by Pt oxidation states (or the relative ratio). The highest HER activity was observed for the support with higher Pt(II) species. When Pt(IV) species were higher on the Ti support, the activity was observed to be poorer. The Ti support with Pt(0) species showed somewhat less activity, compared with the support with Pt(II) species. On the basis of the results, the oxidation state of Pt determines ΔG_{HX} and consequently affects the HER activity. This needs further investigation. In addition to this Pt oxidation state, the thickness of TiO_2 overlayer is an important factor as depicted in Figure 7. The thick TiO_2 layer for the 700 °C-treated samples exhibited poor electrical current to result in low HER activity.

4. Conclusions

In summary, Pt NPs and sputtered-Pt were loaded on Ti sheets with different oxidation states, and tested for photocatalytic CO_2 reduction in a closed reaction chamber and electrochemical hydrogen evolution reaction. Two different demonstration tests were performed to precisely examine the roles of Pt and Ti supports in different application areas. XPS studies confirmed that Pt NP were mainly metallic Pt(0) oxidation state, while sputter-deposited Pt were both Pt(II)-O and Pt(IV)-O species. Ti support before thermal annealing showed oxidation states of Ti(II), Ti(III), and Ti(IV) while the thermal (400 and 700 °C)-annealed Ti showed only the Ti(IV) oxidation state. The CO_2 reduction products were commonly observed to be CO, CH_4, and CH_3OH, and the Pt-free Ti (700 °C) sample showed total yields of up to 87.3, 88.0, 26.9 ppm for the formation of CO, CH_4, and CH_3OH, respectively under UVC irradiation for 13 h. For bare Pt-free Ti substrates, the activity showed the order of Ti (400 °C) <Ti < bare Ti (700 °C). Pt-loading commonly negated the CO_2 reduction yields, but CH_4 selectivity was found to be increased. For electrochemical hydrogen evolution reaction (HER), the Ti (700 °C) support showed the poorest activity and the HER CDs commonly showed the order of Ti (700 °C) < Ti < bare Ti (400 °C), whose order was inverse to the CO_2 reduction. The Ti (700 °C) support showed poorest HER activity, although Pt was loaded on the support. The Ti (400 °C) support showed the highest HER activity increased upon Pt-loading. HER CDs were observed to be 0.1, 9.6, and 10.5 mA/cm^2 at −0.5 V (vs. Ag/AgCl) for bare Ti (400 °C), Pt NP/Ti (400 °C) and Pt-sp/Ti (400 °C), respectively. Sputtered Pt-loaded samples showed a higher activity than the corresponding Pt NP-loaded samples. Conclusively, CO_2 reduction and electrochemical HER activities were mainly determined by the nature of Ti support and Pt oxidation (0,II,IV) species. The present demonstration tests provide valuable information on the design of Pt-overlayer metals and Ti-supports for energy and the environment.

Author Contributions: J.H.Y. performed the CO_2 reduction and HER experiments; S.J.P. performed the XPS experiments; C.K.R. designed the experimental concepts; Y.S. designed the experiments and wrote the paper. All authors have read and agreed to the published version of the manuscript.

Conflicts of Interest: The authors declare no conflict of interest.

References

1. Sohn, Y.; Huang, W.; Taghipour, F. Recent progress and perspectives in the photocatalytic CO_2 reduction of Ti-oxide-based nanomaterials. *Appl. Surf. Sci.* **2017**, *396*, 1696–1711. [CrossRef]
2. Ola, O.; Maroto-Valer, M.M. Review of material design and reactor engineering on TiO_2 photocatalysis for CO_2 reduction. *J. Photochem. Photobiol. C: Photochem. Rev.* **2015**, *24*, 16–42. [CrossRef]
3. Wang, C.; Sun, Z.; Zheng, Y.; Hu, Y.H. Recent progress in visible light photocatalytic conversion of carbon dioxide. *J. Mater. Chem. A* **2019**, *7*, 865–887. [CrossRef]

4. Almomani, F.; Bhosale, R.; Khraisheh, M.; Kumar, A.; Tawalbeh, M. Photocatalytic conversion of CO_2 and H_2O to useful fuels by nanostructured composite catalysis. *Appl. Surf. Sci.* **2019**, *483*, 363–372. [CrossRef]

5. Ali, S.; Flores, M.C.; Razzaq, A.; Sorcar, S.; Hiragond, C.B.; Kim, H.R.; Park, Y.H.; Hwang, Y.; Kim, H.S.; Kim, H.; et al. Gas phase photocatalytic CO_2 reduction, "A brief overview for benchmarking". *Catalysts* **2019**, *9*, 727. [CrossRef]

6. Qiu, H.; Ma, X.; Sun, C.; Zhao, B.; Chen, F. Surface oxygen vacancies enriched Pt/TiO_2 synthesized with a defect migration strategy for superior photocatalytic activity. *Appl. Surf. Sci.* **2020**, *506*, 145021. [CrossRef]

7. Liu, L.; Jiang, Y.; Zhao, H.; Chen, J.; Cheng, J.; Yang, K.; Li, Y. Engineering coexposed {001} and {101} Facets in oxygen-deficient TiO_2 nanocrystals for enhanced CO_2 photoreduction under visible light. *ACS Catal.* **2016**, *6*, 1097–1108. [CrossRef]

8. Ulmer, U.; Dingle, T.; Duchesne, P.N.; Morris, R.H.; Tavasoli, A.; Wood, T.; Ozin, G.A. Fundamentals and applications of photocatalytic CO_2 methanation. *Nat. Commun.* **2019**, *10*, 3169. [CrossRef]

9. Li, X.; Yu, J.; Jaroniec, M.; Chen, X. Cocatalysts for selective photoreduction of CO_2 into solar fuels. *Chem. Rev.* **2019**, *119*, 3962–4179. [CrossRef]

10. Zhang, Z.; Wang, Z.; Cao, S.-W.; Xue, C. Au/Pt nanoparticle-decorated TiO_2 nanofibers with plasmon-enhanced photocatalytic activities for solar-to-fuel conversion. *J. Phys. Chem. C* **2013**, *117*, 25939–25947. [CrossRef]

11. Iyemperumal, S.K.; Pham, T.D.; Bauer, J.; Deskins, N. Quantifying support interactions and reactivity trends of single metal atom catalysts over TiO_2. *J. Phys. Chem. C* **2018**, *122*, 25274–25289.

12. Sim, L.C.; Leong, K.H.; Saravanan, P.; Ibrahim, S. Rapid thermal reduced graphene oxide/Pt–TiO_2 nanotube arrays for enhanced visible-light-driven photocatalytic reduction of CO_2. *Appl. Surf. Sci.* **2015**, *358*, 122–129.

13. Kumaravel, V.; Mathew, S.; Bartlett, J.; Pillai, S.C. Photocatalytic hydrogen production using metal doped TiO_2: A review of recent advances. *Appl. Catal. B Environ.* **2019**, *244*, 1021–1064.

14. Fajrina, N.; Tahir, M. A critical review in strategies to improve photocatalytic water splitting towards hydrogen production. *Int. J. Hydrogen Energy* **2019**, *44*, 540–577.

15. Ahmed, M.; Dincer, I. A review on photoelectrochemical hydrogen production systems: Challenges and future directions. *Int. J. Hydrogen Energy* **2019**, *44*, 2474–2507.

16. Shen, R.; Jiang, C.; Xiang, Q.; Xie, J.; Li, X. Surface and interface engineering of hierarchical photocatalysts. *Appl. Surf. Sci.* **2019**, *471*, 43–87.

17. Bazzo, A.; Urakawa, A. Origin of photocatalytic activity in continuous gas phase CO_2 reduction over Pt/TiO_2. *ChemSusChem* **2013**, *6*, 2095–2102.

18. Tasbihi, M.; Schwarze, M.; Edelmannová, M.; Spoeri, C.; Strasser, P.; Schomäcker, R. Photocatalytic reduction of CO_2 to hydrocarbons by using photodeposited Pt nanoparticles on carbon-doped titania. *Catal. Today* **2019**, *328*, 8–14.

19. Fang, B.; Bonakdarpour, A.; Reilly, K.; Xing, Y.; Taghipour, F.; Wilkinson, D.P. Large-scale synthesis of TiO_2 microspheres with hierarchical nanostructure for highly efficient photodriven reduction of CO_2 to CH_4. *ACS Appl. Mater. Interfaces* **2014**, *6*, 15488–15498.

20. Liu, Y.; Miao, C.; Yang, P.; He, Y.; Feng, J.; Li, D. Synergetic promotional effect of oxygen vacancy-rich ultrathin TiO_2 and photochemical induced highly dispersed Pt for photoreduction of CO_2 with H_2O. *Appl. Catal. B: Environ.* **2019**, *244*, 919–930.

21. Zhang, Q.-H.; Han, W.-D.; Hong, Y.-J.; Yu, J. Photocatalytic reduction of CO_2 with H_2O on Pt-loaded TiO_2 catalyst. *Catal. Today* **2009**, *148*, 335–340. [CrossRef]

22. Wang, W.-N.; An, W.-J.; Ramalingam, B.; Mukherjee, S.; Niedzwiedzki, D.M.; Gangopadhyay, S.; Biswas, P. Size and structure matter: Enhanced CO_2 photoreduction efficiency by size-resolved ultrafine Pt nanoparticles on TiO_2 Single Crystals. *J. Am. Chem. Soc.* **2012**, *134*, 11276–11281. [CrossRef] [PubMed]

23. Kometani, N.; Hirata, S.; Chikada, M. Photocatalytic reduction of CO_2 by Pt-loaded TiO_2 in the mixture of sub- and supercritical water and CO_2. *J. Supercrit. Fluids* **2017**, *120*, 443–447. [CrossRef]

24. Wang, Y.; Lai, Q.; Zhang, F.; Shen, X.; Fan, M.; He, Y.; Ren, S. High efficiency photocatalytic conversion of CO_2 with H_2O over Pt/TiO_2 nanoparticles. *RSC Adv.* **2014**, *4*, 44442–44451. [CrossRef]

25. Singhal, N.; Kumar, U. Noble metal modified TiO_2: Selective photoreduction of CO_2 to hydrocarbons. *Mol. Catal.* **2017**, *439*, 91–99. [CrossRef]

26. Xiong, Z.; Lei, Z.; Chen, X.; Gong, B.; Zhao, Y.; Zhang, J.; Zheng, C.; Wu, J.C.S. CO_2 photocatalytic reduction over Pt deposited TiO_2 nanocrystals with coexposed {101} and {001} facets: Effect of deposition method and Pt precursors. *Catal. Commun.* **2017**, *96*, 1–5. [CrossRef]

27. Mao, J.; Ye, L.; Li, K.; Zhang, X.; Liu, J.; Peng, T.; Zan, L. Pt-loading reverses the photocatalytic activity order of anatase TiO_2 {001} and {010} facets for photoreduction of CO_2 to CH_4. *Appl. Catal. B* **2014**, *144*, 855–862. [CrossRef]

28. Li, F.; Gu, Q.; Niu, Y.; Wang, R.; Tong, Y.; Zhu, S.; Zhang, H.; Zhang, Z.; Wang, X. Hydrogen evolution from aqueous-phase photocatalytic reforming of ethylene glycol over Pt/TiO_2 catalysts: Role of Pt and product distribution. *Appl. Surf. Sci.* **2017**, *391*, 251–258. [CrossRef]

29. Yu, L.; Shao, Y.; Li, D. Direct combination of hydrogen evolution from water and methane conversion in a photocatalytic system over Pt/TiO_2. *Appl. Catal. B: Environ.* **2017**, *204*, 216–223. [CrossRef]

30. Zhang, L.; Pan, N.; Lin, S. Influence of Pt deposition on water-splitting hydrogen generation by highly-ordered TiO_2 nanotube arrays. *Int. J. Hydrogen Energy* **2014**, *39*, 13474–13480. [CrossRef]

31. Serrano, D.; Calleja, G.; Pizarro, P.; Galvez, P. Enhanced photocatalytic hydrogen production by improving the Pt dispersion over mesostructured TiO_2. *Int. J. Hydrogen Energy* **2014**, *39*, 4812–4819. [CrossRef]

32. Košević, M.G.; Zarić, M.M.; Stopic, S.; Stevanović, J.S.; Weirich, T.E.; Friedrich, B.; Panić, V.V. Structural and electrochemical properties of nesting and core/shell Pt/TiO_2 spherical particles synthesized by ultrasonic spray pyrolysis. *Metals* **2020**, *10*, 11. [CrossRef]

33. Lian, Z.; Wang, W.; Li, G.; Tian, F.; Schanze, K.S.; Li, H. Pt-enhanced mesoporous Ti^{3+}/TiO_2 with rapid bulk to surface electron transfer for photocatalytic hydrogen evolution. *ACS Appl. Mater. Interfaces* **2017**, *9*, 16959–16966. [CrossRef]

34. Ordoño, M.B.; Urakawa, A. Active surface species ruling product selectivity in photocatalytic CO_2 reduction over Pt- or Co-promoted TiO_2. *J. Phys. Chem. C* **2019**, *123*, 4140–4147. [CrossRef]

35. Tasbihi, M.; Kočí, K.; Edelmannová, M.; Troppová, I.; Reli, M.; Schomäcker, R. Pt/TiO_2 photocatalysts deposited on commercial support for photocatalytic reduction of CO_2. *J. Photochem. Photobiol. A Chem.* **2018**, *366*, 72–80. [CrossRef]

36. Li, Q.Y.; Zong, L.L.; Li, C.; Cao, Y.H.; Wang, X.D.; Yang, J.J. Photocatalytic reduction of CO_2 to methane on Pt/TiO_2 nanosheet porous film. *Adv. Cond. Matter Phys.* **2014**, *2014*, 316589.

37. Xiong, Z.; Wang, H.; Xu, N.; Li, H.; Fang, B.; Zhao, Y.; Zhang, J.; Zheng, C. Photocatalytic reduction of CO_2 on Pt^{2+}–Pt/TiO_2 nanoparticles under UV/Vis light irradiation: A combination of Pt^{2+} doping and Pt nanoparticles deposition. *Int. J. Hydrogen Energy* **2015**, *40*, 10049–10062. [CrossRef]

38. Li, N.; Chen, Y.; Abanades, S.; Zhang, Z. Enhanced activity of TiO_2 by concentrating light for photoreduction of CO_2 with H_2O to CH_4. *Catal. Commun.* **2018**, *113*, 6–9. [CrossRef]

39. Wang, R.; Shen, J.; Sun, K.; Tang, H.; Liu, Q. Enhancement in photocatalytic activity of CO_2 reduction to CH_4 by 0D/2D Au/TiO_2 plasmon heterojunction. *Appl. Surf. Sci.* **2019**, *493*, 1142–1149. [CrossRef]

40. Naumkin, A.V.; Kraut-Vass, A.; Gaarenstroom, S.W.; Powell, C.J. NIST Standard Reference Database 20, Version 4.1. 2012. Available online: https://srdata.nist.gov/xps/ (accessed on 31 July 2020).

41. Wang, Z.; Huang, L.; Su, B.; Xu, J.; Ding, Z.; Wang, S. Unravelling the promotional effect of La_2O_3 in $Pt/La-TiO_2$ catalysts for CO_2 hydrogenation. *Chem. Eur. J.* **2019**, *26*, 517–523. [CrossRef]

42. Cheng, X.; Li, Y.; Zheng, L.; Yan, Y.; Zhang, Y.-F.; Chen, G.; Sun, S.; Zhang, J. Highly active, stable oxidized platinum clusters as electrocatalysts for the hydrogen evolution reaction. *Energy Environ. Sci.* **2017**, *10*, 2450–2458. [CrossRef]

43. Hong, S.; Rhee, C.K.; Sohn, Y. Photoelectrochemical hydrogen evolution and CO_2 reduction over MoS_2/Si and $MoSe_2/Si$ nanostructures by combined photoelectrochemical deposition and rapid-thermal annealing process. *Catalysts* **2019**, *9*, 494. [CrossRef]

44. Gutić, S.J.; Dobrota, A.S.; Fako, E.; Skorodumova, N.V.; Lopez, N.; Pašti, I.A. Hydrogen evolution reaction-from single crystal to single atom catalysts. *Catalysts* **2020**, *10*, 290. [CrossRef]

45. Yu, F.; Liu, M.; Ma, C.; Di, L.; Dai, B.; Zhang, L.L. A Review on the promising plasma-assisted preparation of electrocatalysts. *Nanomaterials* **2019**, *10*, 1436. [CrossRef]